

# O, S, and N Bridged Atoms Screening on 2D Conjugated Central Units of High-Performance Acceptors

Xiangjian Cao, Zheng Xu, Ruohan Wang, Jiaxin Guo, Wenkai Zhao, Yu Zhang, Zhaoyang Yao,\* Yaxiao Guo, Guankui Long, Xiangjian Wan, and Yongsheng Chen\*

Almost all of central cores in high-performance acceptors are limited to the electron-withdrawing diimide structure currently, which constrains further acceptor structural innovation greatly. Herein, oxygen (O), sulfur (S), and nitrogen (N) atoms are adopted to bridge the 2D conjugated central cores, yielding three acceptor platforms of CH—O, CH—S, and CH—N that differ in structure by only two atoms. Because of the characteristic atomic outer electron configuration and hybrid orbital orientation, O-, S-, and N-bridged central cores display quite different conformations and electronic properties, namely, dibenzodioxin (planar, non-aromatic), thianthrene (puckered, non-aromatic) and phenazine (planar, aromatic), respectively. A systematic investigation discloses how the central core, especially its  $p$ - $\pi$  orbital overlap between lone pair on O/S/N and coterminous benzene planes, affect the intrinsic photoelectronic properties of acceptors for the first time. Finally, CH—N-based binary device affords the highest fill factor of 83.13% in organic photovoltaics along with a first-class efficiency of 20.23%. By evaluating the strictly controlled O-, S-, and N-bridged molecular platforms comprehensively, the work reveals the potential uniqueness of diimide in determining the excellent photovoltaic outcomes of acceptors.

## 1. Introduction

Benefitting from the surging development of small molecular acceptors (SMAs),<sup>[1]</sup> especially for Y-series acceptors,<sup>[2]</sup> organic solar cells (OSCs) have broken through the power conversion efficiency (PCE) bottleneck of 20% recently.<sup>[3]</sup> Such a great achievement primarily relies on the desired 3D molecular packing network of SMAs<sup>[4]</sup> and the superior photodynamic possesses in OSCs.<sup>[5]</sup> It is worth noting that the central cores (for example, benzothiadiazole in Y6,<sup>[2a]</sup> quinoxaline in AQX-2,<sup>[6]</sup> and phenazine in CH22,<sup>[7]</sup> etc. in Figure S1, Supporting Information) contribute a lot to constructing the 3D molecular packing network of SMAs.<sup>[8]</sup> Nevertheless, very rare candidates have been explored as central cores successfully at present except those contain the electron-withdrawing diimide structure.<sup>[9]</sup> This was largely caused by the huge challenge of constructing novel heterocycles for central core which requires both the ease of synthesis and the favorable electronic property.<sup>[10]</sup> In particular, due to

the lack of strictly controlled molecules, the uniqueness of diimide structure in determining the excellent photovoltaic outcomes of SMAs has not been revealed, rendering the eager curiosity in replacing aryl diimide with other moieties, for example, aryl diol or dithiol derivatives that contains the widely applied electron-donating heteroatoms of oxygen (O) and sulfur (S) in organic semiconductors.

In this work, O, S, and nitrogen (N) atoms were adopted to bridge the 2D conjugated central cores (Figure 1a) on the same molecular platform, thus yielding three SMAs of CH—O, CH—S, and CH—N that differ in structure by only two atoms (Figure 1b). Given the vital role of central halogenation in ameliorating nanoscale morphology of donor/acceptor (D/A) blends,<sup>[11]</sup> the four active sites on outer benzene of central units were fully fluorinated. Due to the characteristic atomic outer electron configuration and hybrid orbital orientation, O-, S-, and N-bridged central cores display quite different conformations and electronic properties. A comprehensively and fairly evaluation on these strictly controlled SMAs disclosed how the central core, especially its  $p$ - $\pi$  orbital overlap between lone pair on O/S/N and coterminous benzene planes, affects the intrinsic photoelectronic properties of SMAs. As for the most concerned photovoltaic

X. Cao, Z. Xu, R. Wang, J. Guo, Y. Zhang, Z. Yao, X. Wan, Y. Chen  
 State Key Laboratory and Institute of Elemento-Organic Chemistry  
 The Centre of Nanoscale Science and Technology and Key Laboratory of  
 Functional Polymer Materials  
 Renewable Energy Conversion and Storage Center (RECAST)  
 Frontiers Science Center for New Organic Matter  
 College of Chemistry  
 Nankai University  
 Tianjin 300071, China  
 E-mail: [zyao@nankai.edu.cn](mailto:zyao@nankai.edu.cn); [yschen99@nankai.edu.cn](mailto:yschen99@nankai.edu.cn)

Y. Guo  
 State Key Laboratory of Separation Membranes and Membrane Processes  
 School of Chemistry  
 Tiangong University  
 Tianjin 300387, China

W. Zhao, G. Long  
 School of Materials Science and Engineering  
 National Institute for Advanced Materials  
 Renewable Energy Conversion and Storage Center (RECAST)  
 Nankai University  
 Tianjin 300350, China

The ORCID identification number(s) for the author(s) of this article can be found under <https://doi.org/10.1002/adma.202503131>

DOI: 10.1002/adma.202503131

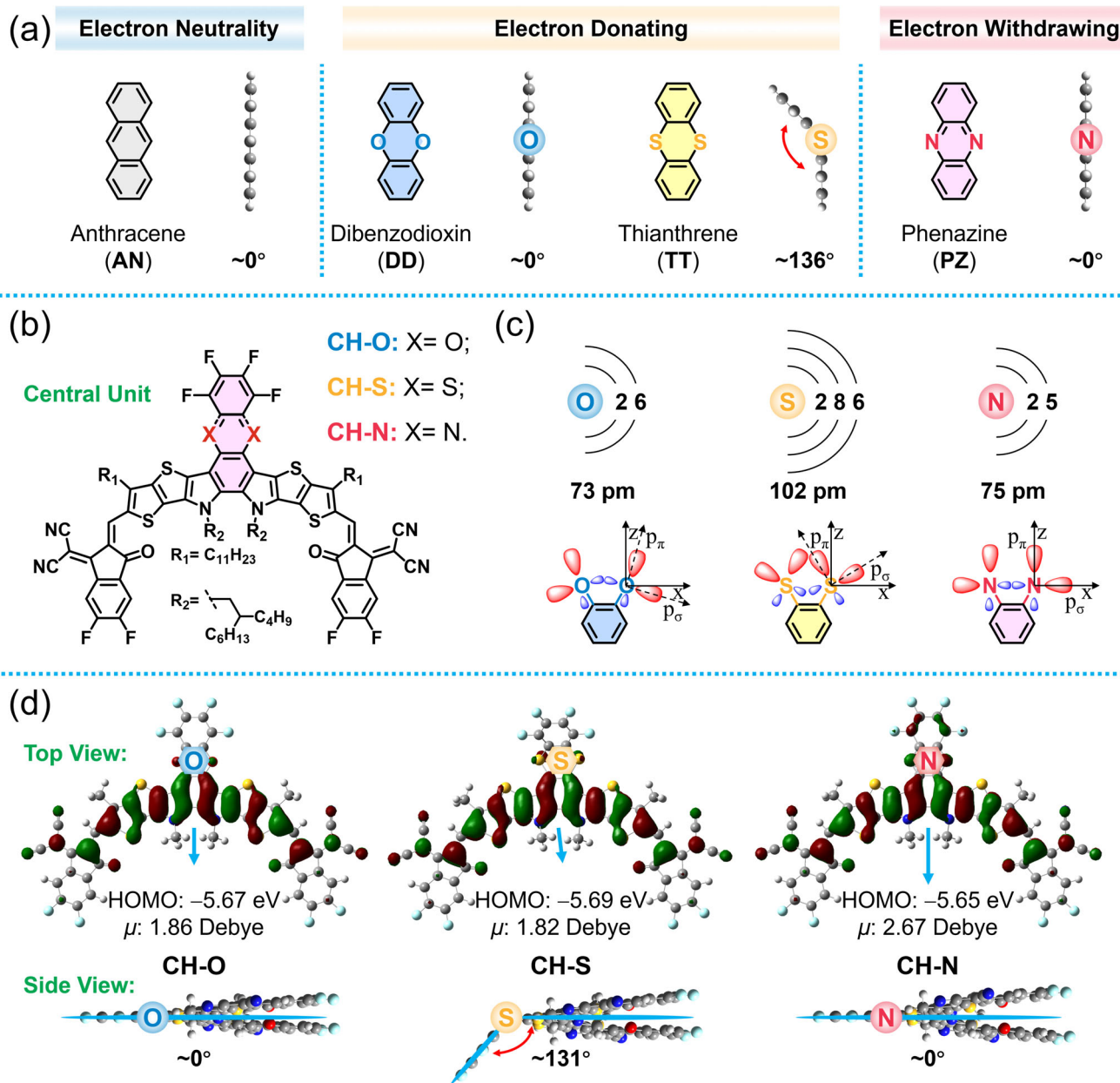


**Figure 1.** a) O-, S-, and N-bridged central cores and their configurational/electronic properties. b) Chemical structure of CH-O, CH-S, and CH-N. c) Atomic radius of O, S, and N elements and schematic diagram showing  $p$ - $\pi$  conjugation in dibenzodioxin, thianthrene, and phenazine. d) Distribution of HOMOs, dipole moments for SMAs and dihedral angles between two benzene planes in dibenzodioxin/thianthrene/phenazine units.

performance, D18:CH-N-based binary OSCs give rise to a first-class efficiency of 20.23% comparing to that of 18.48% for D18:CH-O and 18.93% for D18:CH-S. Note that CH-N has demonstrated the few SMA skeletons besides the path-breaking Y6, L8-BO, and BTP-eC9 etc., which could boost PCE of binary OSCs surpassing 20%.<sup>[12]</sup> More excitingly, D18:CH-N-based binary OSCs have also reached the highest fill factor (FF) of 83.13% in organic photovoltaics, manifesting the FF gap between organic and inorganic photovoltaics can be significantly narrowed through rational tailoring of SMAs.

## 2. Results and Discussion

In light of almost the same molecular backbones of CH-O, CH-S, and CH-N, the differences of their photoelectric properties will be largely determined by the bridged atoms on central units. Therefore, we built a detailed **Table 1** to provide a clear landscape for molecular comparison at atomic, central unit and SMA levels. We first investigated the central units of SMAs, which are extracted as O-containing dibenzodioxin for CH-O, S-containing thianthrene for CH-S and N-containing phenazine for CH-N (Figure 1a). For the N-bridged phenazine, the outer

**Table 1.** A Parameters Summary of Physicochemical Property from Bridged Atoms, Central Cores to SMAs.

Bridged atoms			
Element Symbol	O	S	N
Atomic Radius	73 pm	102 pm	75 pm
Electronegativity	3.44	2.58	3.04
Outer Electron Configuration	2s <sup>2</sup> 2p <sup>4</sup>	3s <sup>2</sup> 3p <sup>4</sup>	2s <sup>2</sup> 2p <sup>3</sup>
Central units			
Name	Dibenzodioxin	Thianthrene	Phenazine
Hybridization of Bridged Atoms	Likely sp <sup>2</sup>	Likely sp <sup>2</sup>	sp <sup>2</sup>
p- $\pi$ Overlap <sup>a)</sup>	Moderate	Small	Large
Bond Length (C–X) <sup>b)</sup>	$\approx$ 1.38 Å	$\approx$ 1.79 Å	$\approx$ 1.34 Å
Conformation	Quasi-Planar	Puckered	Quasi-Planar
Dihedral Angle <sup>b)</sup>	$\approx$ 0 Degree	$\approx$ 136 Degree	$\approx$ 0 Degree
C–X–C Bond Angle <sup>b)</sup>	$\approx$ 116 Degree	$\approx$ 101 Degree	$\approx$ 117 Degree
Aromaticity	Non-Aromatic	Non-Aromatic	Aromatic
Symmetry Class	D <sub>2h</sub>	C <sub>2v</sub>	D <sub>2h</sub>
SMAs			
Name	CH–O	CH–S	CH–N
Bond Length (C–X) <sup>c)</sup>	$\approx$ 1.39 Å ( $\approx$ 1.38 Å)	$\approx$ 1.79 Å ( $\approx$ 1.78 Å)	$\approx$ 1.35 Å ( $\approx$ 1.34 Å)
Dihedral Angle <sup>c)</sup>	$\approx$ 0 Degree ( $\approx$ 0 Degree)	$\approx$ 131 Degree ( $\approx$ 131 Degree)	$\approx$ 0 Degree ( $\approx$ 0 Degree)
C–X–C Bond Angle <sup>c)</sup>	$\approx$ 114 Degree ( $\approx$ 115 Degree)	$\approx$ 100 Degree ( $\approx$ 100 Degree)	$\approx$ 115 Degree ( $\approx$ 117 Degree)
HOMO <sub>Cal</sub> <sup>d)</sup>	–5.67 eV	–5.69 eV	–5.65 eV
LUMO <sub>Cal</sub> <sup>d)</sup>	–3.56 eV	–3.57 eV	–3.60 eV
HOMO <sub>UPS</sub> <sup>e)</sup>	–5.72 eV	–5.71 eV	–5.70 eV
LUMO <sub>UPS</sub> <sup>e)</sup>	–4.28 eV	–4.28 eV	–4.30 eV
HOMO Distribution	S, N-Heteroacene	S, N-Heteroacene and S	S, N-Heteroacene and N
LUMO Distribution	S, N-Heteroacene, most on Cyano	S, N-Heteroacene, most on Cyano	S, N-Heteroacene, most on Cyano
Polarizability <sub>Cal</sub>	1238 Bohr <sup>3</sup>	1262 Bohr <sup>3</sup>	1312 Bohr <sup>3</sup>
Dipole Moment <sub>Cal</sub>	1.86 Debye	1.82 Debye	2.67 Debye
$\lambda_{Cal}$ <sup>f)</sup>	700 nm	696 nm	721 nm
Oscillator Strength <sub>Cal</sub>	2.20	2.13	2.28
$\lambda_{solution}$	715 nm	710 nm	729 nm
$\lambda_{film}$	783 nm	788 nm	805 nm
$\Delta\lambda$ <sup>g)</sup>	68 nm	78 nm	76 nm
Optical Bandgap <sub>film</sub>	1.44 eV	1.43 eV	1.40 eV
$\epsilon_{solution}$ <sup>h)</sup>	$1.81 \times 10^5$ M <sup>–1</sup> cm <sup>–1</sup>	$1.68 \times 10^5$ M <sup>–1</sup> cm <sup>–1</sup>	$2.22 \times 10^5$ M <sup>–1</sup> cm <sup>–1</sup>
$\epsilon_{film}$ <sup>i)</sup>	$1.36 \times 10^5$ cm <sup>–1</sup>	$1.25 \times 10^5$ cm <sup>–1</sup>	$1.47 \times 10^5$ cm <sup>–1</sup>
Stokes Shift <sub>solution</sub>	44 nm	42 nm	38 nm
d <sub><math>\pi</math>–<math>\pi</math></sub> (GIWAXS)	3.57 Å	3.63 Å	3.55 Å
CCL (GIWAXS)	23.6 Å	21.8 Å	24.6 Å
d <sub><math>\pi</math>–<math>\pi</math></sub> (Crystal)	3.38 Å	N/A	3.35 Å
$\mu_e$ <sup>j)</sup>	$1.3 \times 10^{-4}$ cm <sup>2</sup> V <sup>–1</sup> s <sup>–1</sup>	$1.1 \times 10^{-4}$ cm <sup>2</sup> V <sup>–1</sup> s <sup>–1</sup>	$6.2 \times 10^{-4}$ cm <sup>2</sup> V <sup>–1</sup> s <sup>–1</sup>
Exciton Lifetime <sub>film</sub>	1.0 ns	1.4 ns	1.3 ns
PLQY <sup>k)</sup>	5.0%	10.9%	8.9%
$\epsilon_r$	2.7	2.6	2.9
E <sub>b</sub> <sup>l)</sup>	48 meV	40 meV	56 meV

a) The p<sub>z</sub> orbital of bridged atoms and adjacent benzenes; b) Dihedral angles of the two benzene rings derived from DFT calculations; c) The average crystallographic data of central units, and the values marked in the parentheses derived from DFT calculations; d) HOMO/LUMO calculated by DFT; e) HOMO/LUMO derived from UPS measurements and their optical bandgaps; f) The wavelength ( $\lambda$ ) of maximum absorption peaks derived from DFT calculations; g) The maximum absorption wavelength change ( $\Delta\lambda$ ) from solution to film; h) The  $\epsilon$  in solutions; i) The  $\epsilon$  of neat films; j)  $\mu_e$ s of neat films; k) PLQYs of SMAs in solid films; l) E<sub>b</sub>s derived from the temperature dependent PL.

electron configuration of N atom is  $2s^2 2p^3$ . By adopting the  $sp^2$  hybridization, one of valence electrons on N atom remains in the p orbital that is perpendicular to the conjugated skeleton, giving rise to a featured  $\pi_6^6$  system on the central six-ring (Figure S2, Supporting Information). Given the quite larger electronegativity (3.04) of N atom than carbon (C) atom (2.55), the phenazine unit exhibits an electron-withdrawing nature in building SMAs. In our initial expectation, if the O atom on dibenzodioxin or S atom on thianthrene also adopts the  $sp^2$  hybridization (like aryl diol or dithiol), the six valence electrons outside of O ( $2s^2 2p^4$ ) or S ( $3s^2 3p^4$ ) atoms would render a more electron-rich  $\pi_6^8$  system on central six-ring of dibenzodioxin or thianthrene (Figure S2, Supporting Information). In theory, this is expected to upshift the highest occupied molecular orbital (HOMO) energy levels of SMAs and narrow their optical bandgaps further, especially for S atom on thianthrene that possesses a comparable electronegativity (2.58) to C atom (2.55) but much smaller than N atom (3.04). In addition, the larger atomic radius of S (102 pm, Figure 1c) is more easily to be polarized and form the intermolecular non-covalent interactions, just like replacing S with selenium in many high-performance SMA systems,<sup>[13]</sup> which is expected to improve charge transfer/transport in OSCs.<sup>[14]</sup>

Unexpectedly, the HOMOs downshift stepwise from CH–N (–5.65 eV), CH–O (–5.67 eV) to CH–S (–5.69 eV), resulting in the blue-shifting absorptions based on our density functional theory (DFT) calculations (Figure 1d). This confuses us initially until the characteristic hybrid orbital orientations of O, S, and N were considered (Figure 1c). The  $p_z$  or  $p_\pi$  orbital of N atom is perpendicular to the phenazine plane, contributing to a fully conjugated skeleton. In sharp contrast, an insufficient  $p$ - $\pi$  orbitals overlap between  $p_z$  orbital of O and the immediately adjacent benzene could be observed in dibenzodioxin. This may be the root cause that dibenzodioxin could maintain a relatively planar conformation, although it seems to have an anti-aromatic  $4n \pi e^-$  feature.<sup>[15]</sup> As regards to the thianthrene, the angle between the  $p_x$  orbital and benzene plane further decreases, leaving a less overlap of  $p$ - $\pi$  orbitals comparing to dibenzodioxin.<sup>[16]</sup> Moreover, due to the markedly longer C–S bond ( $\approx 1.79$  Å) than C–N ( $\approx 1.34$  Å) or C–O ( $\approx 1.38$  Å), the central ring of thianthrene will suffer from a greater strain than dibenzodioxin or phenazine if a planar conformation is still adapted. As a result, the characteristic puckered conformation of thianthrene with a dihedral angle of  $\approx 131$  degree and a small C–S–C angle of  $\approx 100$  degree (Figure 1d; Table 1) is afforded by both the  $4n \pi e^-$  feature and great ring strain. Note that the fully conjugation of central unit in CH–O and CH–S was broken by the insufficient  $p$ - $\pi$  orbital overlap. This freezes the electron donating ability of O or S and results in the unexpectedly blue-shifted absorption of CH–O and CH–S comparing to CH–N. As shown in Table 1, the polarizabilities of CH–O (1238 Bohr<sup>3</sup>) and CH–S (1262 Bohr<sup>3</sup>) are smaller than that of CH–N (1312 Bohr<sup>3</sup>), which may be caused by the localized valence electrons in p orbitals of O and S but delocalized ones for N. The lowest unoccupied molecular orbitals (LUMOs) of three SMAs show a wide distribution along the whole molecular backbones with the most on the highly electron-withdrawing groups of cyano (Figure S3, Supporting Information). The HOMOs are mainly distributed on the S, N-heteroacene with a small amount on the outer benzene of phenazine, whereas almost no distributions for diben-

zodioxin or thianthrene (Figure 1d), which also manifests the non-aromatic features of dibenzodioxin and thianthrene. As displayed in Figure S4 (Supporting Information), the spatial location of HOMOs and LUMOs determines that all the three SMAs have a favorable acceptor-donor-acceptor (A–D–A) architecture that will help to achieve the superior charge transfer/transport processes in OSCs.<sup>[17]</sup> In addition, a markedly larger dipole moment of 2.67 Debye can be afforded by CH–N with respect to that of 1.86 Debye for CH–O and 1.82 Debye for CH–S (Figure 1d), which is helpful to form an enhanced molecular packing unveiled by some literatures.<sup>[18]</sup>

As presented in Figure 2a,b, the molecular conformations extracted from single crystals are similar to the theoretically predicted ones (please find the detailed crystallographic parameters in Table S1, Supporting Information). Despite the puckered central unit, the thianthrene could still participate in the intermolecular packing greatly and form a desirable 3D molecular packing network.<sup>[20]</sup> Herein, the 3D molecular packing network of CH–S was evidenced by CS2 due to the lack of single crystal of CH–S. The main difference between CH–S and CS2 is the different halogenation on central units (Figure S5, Supporting Information), thereby the quite distinctive puckered molecular conformation of CH–S could be fully maintained in CS2.<sup>[19]</sup> The HOMO/LUMO energy levels are –5.72 / –4.28 eV for CH–O, –5.71 / –4.28 eV for CH–S, and –5.70 / –4.30 eV for CH–N determined by the ultraviolet photoelectron spectroscopy (UPS) measurements and the optical bandgaps (Figure S6, Supporting Information).<sup>[21]</sup> Moreover, the energy level alignment of CH–O, CH–S, and CH–N derived from cyclic voltammetry (CV) measurements is roughly consistent with the DFT predictions and UPS results above (Figure 3a; Figure S7, Supporting Information), showing the obviously upshifted HOMO for CH–N (–5.68 eV) comparing to that of CH–O (–5.75 eV) and CH–S (–5.73 eV). Therefore, the maximum absorption peak ( $\lambda_{\text{solution}}$ ) of CH–N in solutions locates at 729 nm, redshifted by 14 and 19 nm comparing to CH–O and CH–S, respectively (Figure 3b). As regards to films, the wavelengths of maximum absorption peaks ( $\lambda_{\text{film}}$ ) are 783 nm for CH–O, 788 nm for CH–S, and 805 nm for CH–N. Note that the absorption of CH–S is blue-shifted relative to CH–O in solutions, while the opposite is true for thin films due to the larger wavelength change ( $\Delta\lambda$ ) of 78 nm for CH–S, but only 68 nm for CH–O from solutions to films. In general, the steric hindrance from the puckered thianthrene will prevent the compact  $\pi$ - $\pi$  stacking of CH–S,<sup>[22]</sup> thus blue-shifting the maximum absorption peaks in films. Herein, the counterexample suggests that the puckered thianthrene may boost the packing modes of CH–S preferring to J aggregates by weakening the central unit involved molecular packings.<sup>[23]</sup> In addition, the molar extinct coefficient ( $\epsilon$ ) of CH–N in chloroform solutions is  $2.22 \times 10^5 \text{ M}^{-1} \text{ cm}^{-1}$ , larger than that of  $1.81 \times 10^5 \text{ M}^{-1} \text{ cm}^{-1}$  for CH–O and  $1.68 \times 10^5 \text{ M}^{-1} \text{ cm}^{-1}$  for CH–S (Figure 3c). This may be induced by the broader conjugated plane of CH–N and agrees well with its larger oscillator strength comparing to CH–O and CH–N (Table 1). Meanwhile, the  $\epsilon$  in films were also evaluated, being  $1.36 \times 10^5 \text{ cm}^{-1}$  for CH–O,  $1.25 \times 10^5 \text{ cm}^{-1}$  for CH–S and  $1.47 \times 10^5 \text{ cm}^{-1}$  for CH–N (Figure S8, Supporting Information). The larger  $\epsilon$  of CH–N will be beneficial for the sufficient light harvesting even with a thinner active layer.

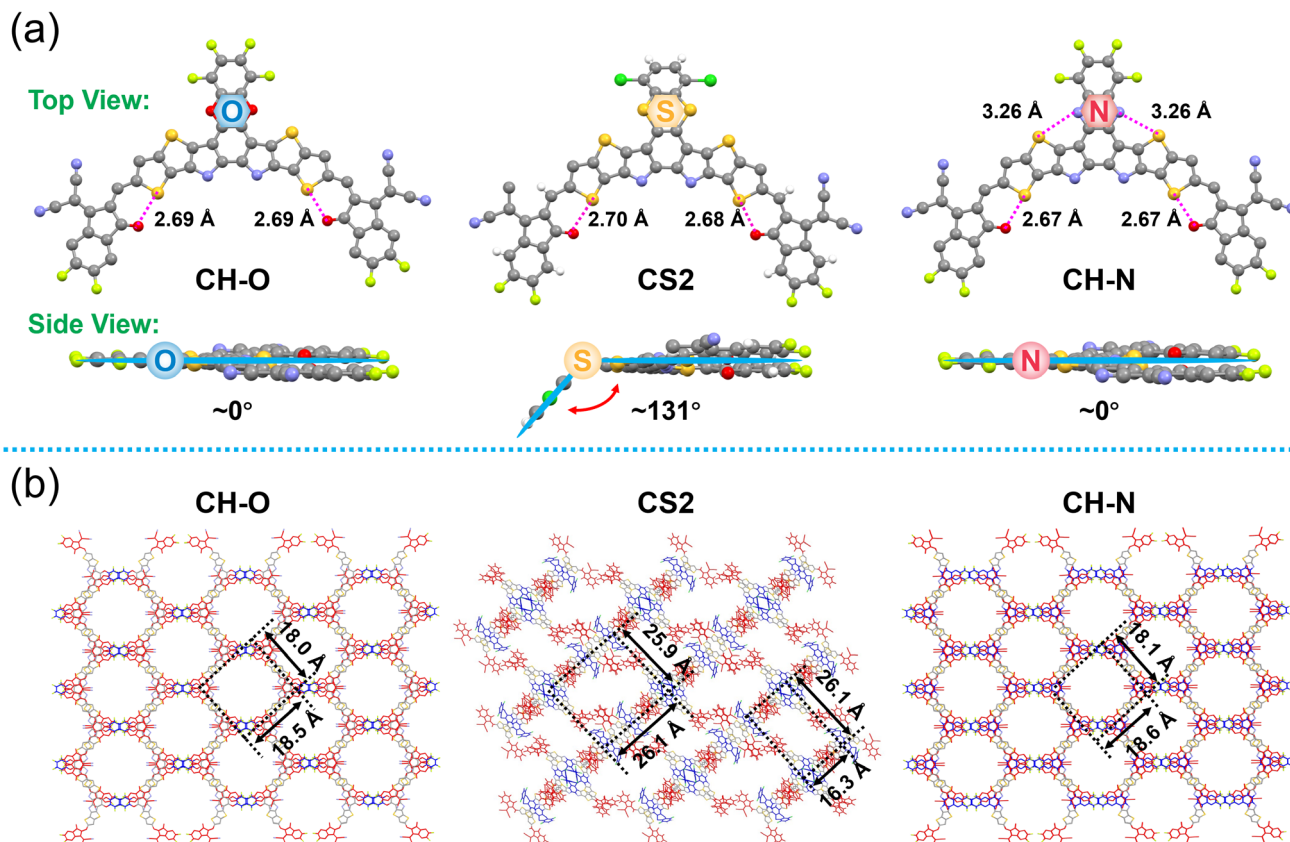


**Figure 2.** a) The molecular conformation and b) molecular packings extracted from single crystals. Herein, CH–S was evidenced by a similar molecule of CS2 that was reported in our previous work.<sup>[19]</sup>

The Stokes shifts of three SMAs were estimated to be 44 nm for CH–O, 42 nm for CH–S, and 38 nm for CH–N (Table 1; Figure S9, Supporting Information), indicative of the probably smaller reorganization energy for CH–N. Note that the decreased reorganization energy is beneficial for the facilitated charge transport and reduced energy losses.<sup>[5a]</sup> The 2D grazing incidence wide angle X-ray scattering (GIWAXS) measurements of neat films were carried out to evaluate the different molecular packing behaviors of three SMAs. Despite the planar or puckered central units, all the three SMAs showed a desired face-on molecular packing orientation (Figure 3d; Figure S10, Supporting Information). The  $\pi$ – $\pi$  stacking distances ( $d_{\pi-\pi}$ ) were roughly estimated as 3.57 Å for CH–O, 3.63 Å for CH–S and 3.55 Å for CH–N. Moreover, the crystal coherence length (CCL) of CH–S (21.8 Å) is also smaller than that of 23.6 Å for CH–O and 24.6 Å for CH–N (Figure 3e; Table S2, Supporting Information). Apparently, the puckered conformation of thianthrene should be responsible for the enlarged  $d_{\pi-\pi}$  and decreased CCL of CH–S. Note that the more compact and ordered molecular packing of CH–N has contributed to a greatly improved electron mobility ( $\mu_e$ ) of  $\approx 6 \times 10^{-4} \text{ cm}^2 \text{ V}^{-1} \text{ s}^{-1}$  comparing to that of  $\approx 1 \times 10^{-4} \text{ cm}^2 \text{ V}^{-1} \text{ s}^{-1}$  for CH–O and CH–S (Figure 3f; Figure S11, Supporting Information). The exciton lifetimes of three SMAs in films were also monitored and calculated as 1.0 ns for CH–O, 1.4 ns for CH–S, and 1.3 ns for CH–N (Figure 3g). Given the similar electronic feature of CH–O and CH–S while the quite different conformations of

central units, the smaller exciton lifetime of CH–O comparing to CH–S may be largely caused by the more extensive aggregation-induced exciton annihilation.<sup>[24]</sup> It is also reasonable to observe the larger photoluminescence quantum yields (PLQY) of 10.9% for CH–S, whereas only 5.0% for CH–O (Figure 3h). The desired exciton/luminescent properties of CH–S comparing to CH–O are conducive to suppressing the non-radiative recombination in resulting OSCs (discussed below).<sup>[25]</sup> The relative dielectric constant ( $\epsilon_r$ ) of organic light-harvesting materials could affect their exciton binding energy ( $E_b$ ) through the following empirical formula of  $E_b = e^2 / (4\pi \epsilon_0 \epsilon_r R)$ ,<sup>[26]</sup> where  $e$  and  $\epsilon_0$  represents the elementary charge and vacuum dielectric constant, respectively;  $R$  is defined as the average electron-hole distance of molecule. The similar  $\epsilon_r$  values  $\approx 2.8$  were observed for three SMAs (Figure S12, Supporting Information) and the  $R$  is also similar in light of the only two atoms difference for CH–O, CH–S, and CH–N structures. This consists with the comparable charge separation energy barriers (similar to  $E_b$ s) of SMAs in range of 40–60 meV (Figure 3i). In fact, the absolute values of  $E_b$  are hard to be obtained through temperature-dependent PL (Figure S13, Supporting Information), thereby only the relative varying tendency between similar molecules is meaningful.

To investigate the difference of photovoltaic performance caused by O, S, and N bridged atoms, we used a well-matched donor of D18<sup>[27]</sup> to blend with SMAs and fabricated OSCs with a conventional device structure. The best  $J$ - $V$  characteristics and

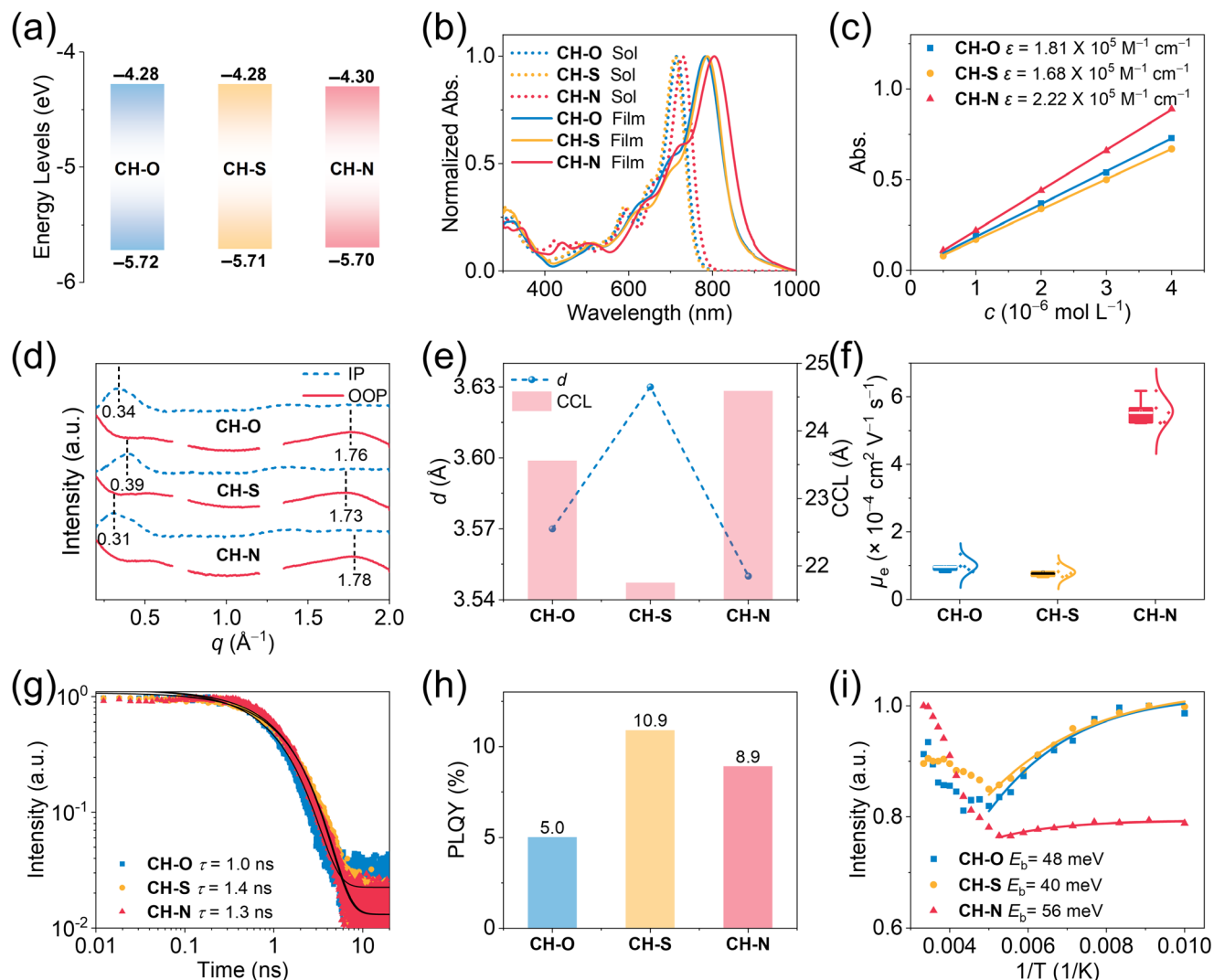


**Figure 3.** a) Energy levels of CH–O, CH–S, and CH–N derived from UPS measurements. b) UV–vis spectra for CH–O, CH–S, and CH–N in chloroform solutions and solid films. c) The  $\epsilon$  of CH–O, CH–S, and CH–N in solutions. d) Line-cut profiles of 2D GIWAXS patterns of CH–O, CH–S, and CH–N neat films. e)  $d_{\pi-\pi}$  and CCLs variation derived from GIWAXS measurements in out of plane direction. f)  $\mu_e$ s of SMAs neat films derived from the space-charge-limited current (SCLC) measurements. g) Time-resolved photoluminescence (PL) decay traces of neat films. h) PLQYs of SMAs in solid films. i)  $E_b$ s derived from the temperature dependent PL.

external quantum efficiency (EQE) spectra were exhibited in **Figure 4a,c** and **Table 2**, respectively. The related data of device optimization were also enumerated in **Tables S3–S5** (Supporting Information).

The binary OSCs based on D18:CH–O exhibited a moderate PCE of 18.48% with an unsatisfied short-circuit current density ( $J_{SC}$ ) of 24.38  $\text{mA cm}^{-2}$ , but the outstanding open-circuit voltage ( $V_{OC}$ ) of 0.942 V and FF of 80.47% (**Figure 4a**; **Table 2**). After replacing the bridged atom O with S, a superior PCE of 18.93% was afforded with a slightly improved  $J_{SC}$  of 24.98  $\text{mA cm}^{-2}$  and FF of 80.86%. Impressively, a first-class PCE of 20.23% was finally achieved by D18:CH–N-based binary OSCs with a significantly improved  $J_{SC}$  of 26.74  $\text{mA cm}^{-2}$  and an exceptional FF of 83.13%. It is noteworthy that the FF of 83.13% is the best value among all of the previously reported OSCs (**Figure 4b**; **Table S6**, Supporting Information). This encouraging result man-

ifests the FF gap between organic and inorganic photovoltaics can be significantly narrowed through rational tailoring of central units of SMAs. Furthermore, CH–N-based OSCs with the 1.0  $\text{cm}^2$  active layer area also realized a good PCE of 17.62% and a high FF of 75.53% (**Figure S14**, Supporting Information). As regards to the long-term stability, the three binary OSCs could maintain  $\approx 95\%$  and  $\approx 85\%$  of their initial PCEs after  $\approx 300$  h testing at room temperature and 65  $^\circ\text{C}$ , respectively. For the photo-stability, D18:CH–O- and D18:CH–N-based OSC kept  $\approx 80\%$  of its initial PCE after  $\approx 250$  h evaluated by the max power point (MPP) tracking test, whereas the D18:CH–S only retained  $\approx 75\%$  of its initial PCE (**Figure S15**, Supporting Information). The integrated  $J_{SC}$ s showed that CH–N-based OSC has an obviously increased value comparing to CH–O- and CH–S-based OSCs (**Figure 4c**), which is mainly caused by its broader photoelectronic response. Meanwhile, the EQE spectrum response

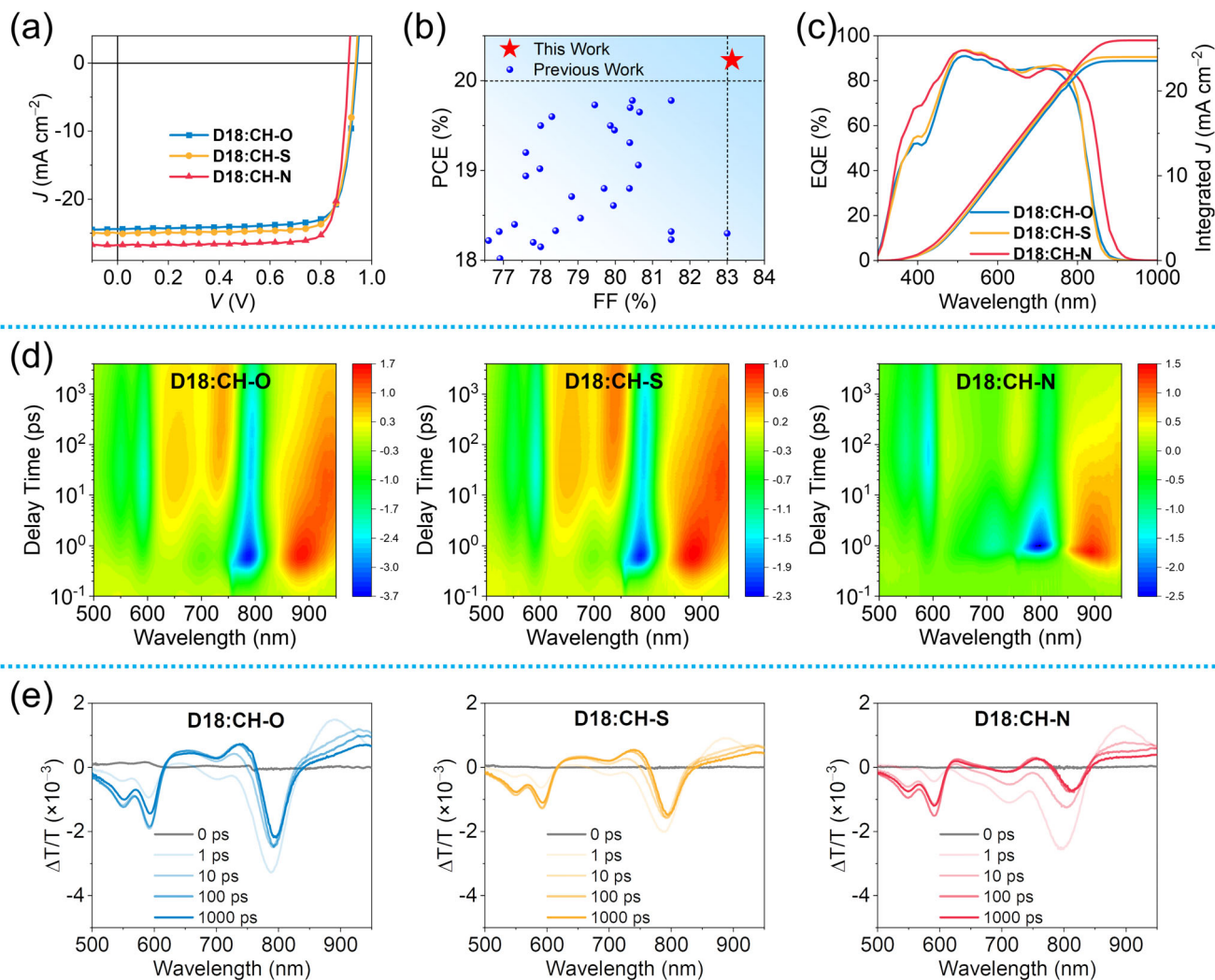


**Figure 4.** a) *J*-*V* curves for champion OSCs. b) Summary of PCE diagram of binary OSCs with bulk-heterojunction (BHJ) structure, showing the best values achieved by this work (Table S6, Supporting Information). c) EQE plots and integrated  $J_{SC}$  curves. d) 2D color plots of TA spectra of D18:CH-O, D18:CH-S, and D18:CH-N blended films under 760 nm excitation. e) Representative TA spectra of the blended films recorded at indicated delay times.

of CH-N-based OSCs is significantly higher than the others  $\approx 400$  nm, which could be mainly attributed to the enhanced light absorption of CH-N films (Figure S8, Supporting Information). The charge dynamic process was further studied by conducting transient absorption (TA) spectroscopy measurements. The 2D TA spectroscopy of blended and neat films were displayed

in Figure 4d and Figure S16 (Supporting Information), respectively, and the corresponding TA spectra at different delay times were shown in Figure 4e. As presented in Figure S16 (Supporting Information), the ground-state bleaching (GSB) signal of SMAs  $\approx 800$  nm appears rapidly after excitation in neat films. While, the GSB signal of D18  $\approx 590$  nm is observed as the decay of GSB

**Table 2.** Summary of photovoltaic parameters for OSCs.

Active layers <sup>a)</sup>	$V_{OC}$ [V]	$J_{SC}$ [ $\text{mA cm}^{-2}$ ]	Cal. $J_{SC}$ <sup>b)</sup> [ $\text{mA cm}^{-2}$ ]	FF [%]	PCE [%]
D18:CH-O	0.942 (0.936 $\pm$ 0.004)	24.38 (24.25 $\pm$ 0.12)	23.54	80.47 (80.36 $\pm$ 0.23)	18.48 (18.24 $\pm$ 0.10)
D18:CH-S	0.937 (0.935 $\pm$ 0.002)	24.98 (24.99 $\pm$ 0.09)	24.00	80.86 (80.60 $\pm$ 0.22)	18.93 (18.84 $\pm$ 0.07)
D18:CH-N	0.910 (0.907 $\pm$ 0.002)	26.74 (26.90 $\pm$ 0.16)	25.96	83.13 (82.56 $\pm$ 0.35)	20.23 (20.15 $\pm$ 0.09)

<sup>a)</sup> Average parameters derived from 15 independent OSCs (Tables S3-S5, Supporting Information); <sup>b)</sup> Current densities by integrating EQE plots.

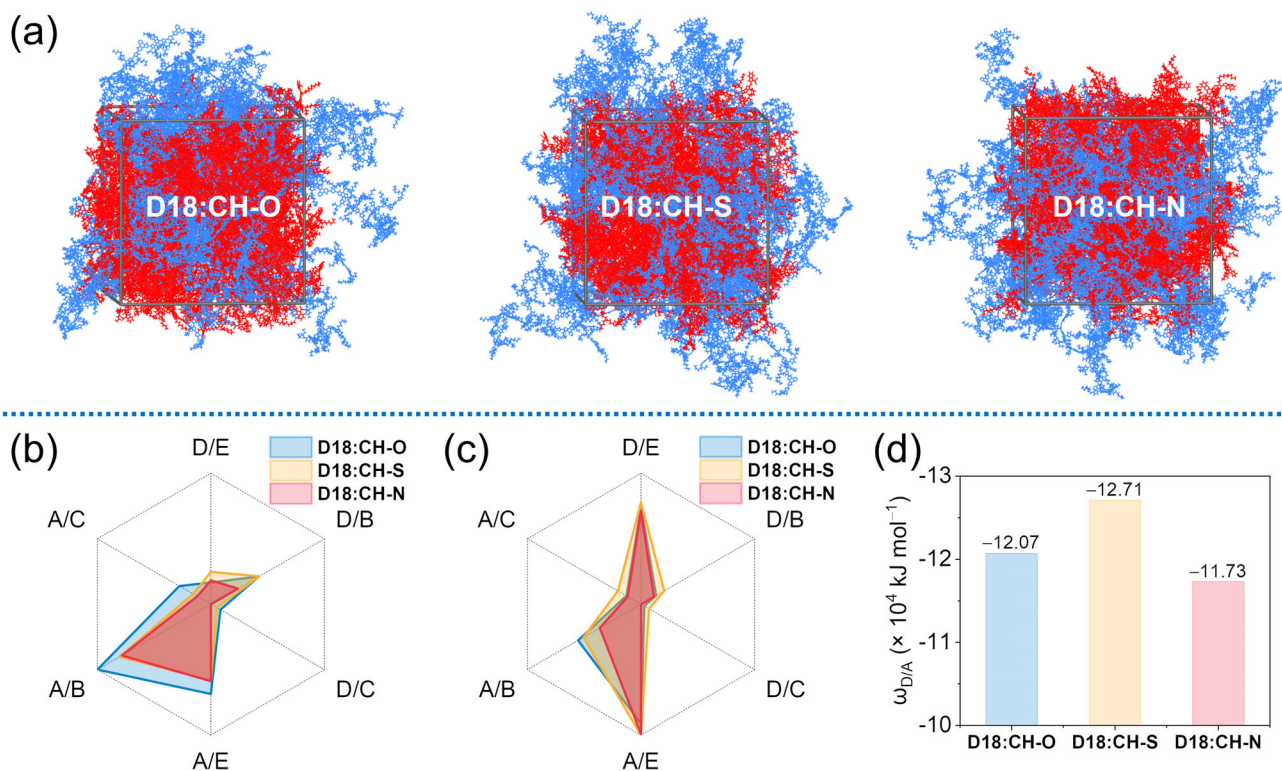


**Figure 5.** a) MD simulation of D18:CH–O, D18:CH–S, and D18:CH–N, where the blue and red colors correspond to D18 and SMAs, respectively. b) Face-on stacking counts comparison of D18:CH–O, D18:CH–S, and D18:CH–N per unit volume. c) Total stacking counts comparison of D18:CH–O, D18:CH–S, and D18:CH–N per unit volume. d) The D/A  $\omega$  were also listed.

signal of SMAs, which manifests the hole transfer occurs from the SMAs to D18 in the blends.<sup>[28]</sup> Therefore, the charge transfer process in D/A blends can be assessed by analyzing the decay dynamics of GSB signals at  $\approx 590$  nm. Based on a biexponential function, the time of exciton dissociation/diffusion ( $\tau_1/\tau_2$ ) were fitted to be 0.60/3.94, 0.63/5.01 and 0.98/11.53 ps for D18:CH–O, D18:CH–S, and D18:CH–N, respectively (Figure S17, Supporting Information). Comparing to its two counterparts, the relatively larger  $\tau_1$  and  $\tau_2$  for D18:CH–N blends indicated the inferior exciton dissociation dynamics. However, D18:CH–N-based OSCs still achieved the best PCE due to the other advantages like the broader absorption range (Figure S8, Supporting Information), reduced energy losses and improved charge transport behaviors (discussed below), etc. Actually, the  $\tau_1/\tau_2$  of D18:CH–N are still at the excellent level among the high-efficient OSCs in the literatures,<sup>[4c,23b,29]</sup> suggesting that the charge transfer process may be not the determining factor to limit CH–N-based OSCs.

It is quite interesting that CH–S-based blend shows superior exciton dissociation dynamics comparing to that of CH–N, especially considering the unique folded molecular geometry for central unit of CH–S but planar for CH–N. Given the exciton dissociation usually occurs at the interface of D/A phase, we carried out the molecular dynamics (MD) simulations of D18:CH–O, D18:CH–S, and D18:CH–N (Figure 5a; Figure S18 and S19, Supporting Information) to illustrate the molecular packing scenarios. As shown in Figure S18 (Supporting Information), D18 was divided into two segments, labeled as donor (D) and accep-

tor (A), while SMAs were divided into three segments, labeled as end (E), bridge (B), and center (C). Six distinct face-on or  $\pi$ - $\pi$  packing conditions were identified as DE, DB, DC, AE, AB and AC (Figure 5b; Table S7, Supporting Information). The total stacking counts of CH–S (205.9) and CH–O (197.0) are slightly larger than that of CH–N (189.9) (Figure 5c; Table S8, Supporting Information), thus contributing the overall enlarged interaction energies ( $\omega$ ) of D18:CH–S ( $-12.7 \times 10^4$  kJ mol<sup>-1</sup>) and D18:CH–O ( $-12.1 \times 10^4$  kJ mol<sup>-1</sup>) comparing to D18:CH–N ( $-11.7 \times 10^4$  kJ mol<sup>-1</sup>) (Figure 5d). This may be one of the reasons why D18:CH–S and D18:CH–O blends could possess the superior exciton dissociation dynamic comparing to D18:CH–N.

By measuring the dependence of  $V_{OC}$  on light intensity (Figure S20, Supporting Information),  $S/(kT/q)$  for D18:CH–O, D18:CH–S, and D18:CH–N-based devices were determined to be 1.32, 1.30, and 1.15, respectively, demonstrating that the trap-assisted recombination was effectively suppressed in CH–N-based device.<sup>[30]</sup> Besides, the energy loss of OSCs decreased from D18:CH–O, D18:CH–S to D18:CH–N, especially for the non-radiative energy loss of  $\Delta E_3$ , being 0.244, 0.238, and 0.214 eV, respectively (Figures S21 and S22; Table S9, Supporting Information). These results manifest the photovoltaic performance of OSCs could be significantly affected by the bridging atoms on 2D conjugated extend central cores of SMAs, moreover, provide a valuable reference for further design of highly efficient SMAs.

To penetrate into the root causes of the record FF observed in CH–N-based devices, the charge transport behaviors in CH–O, CH–S, and CH–N-based blends were evaluated by using the

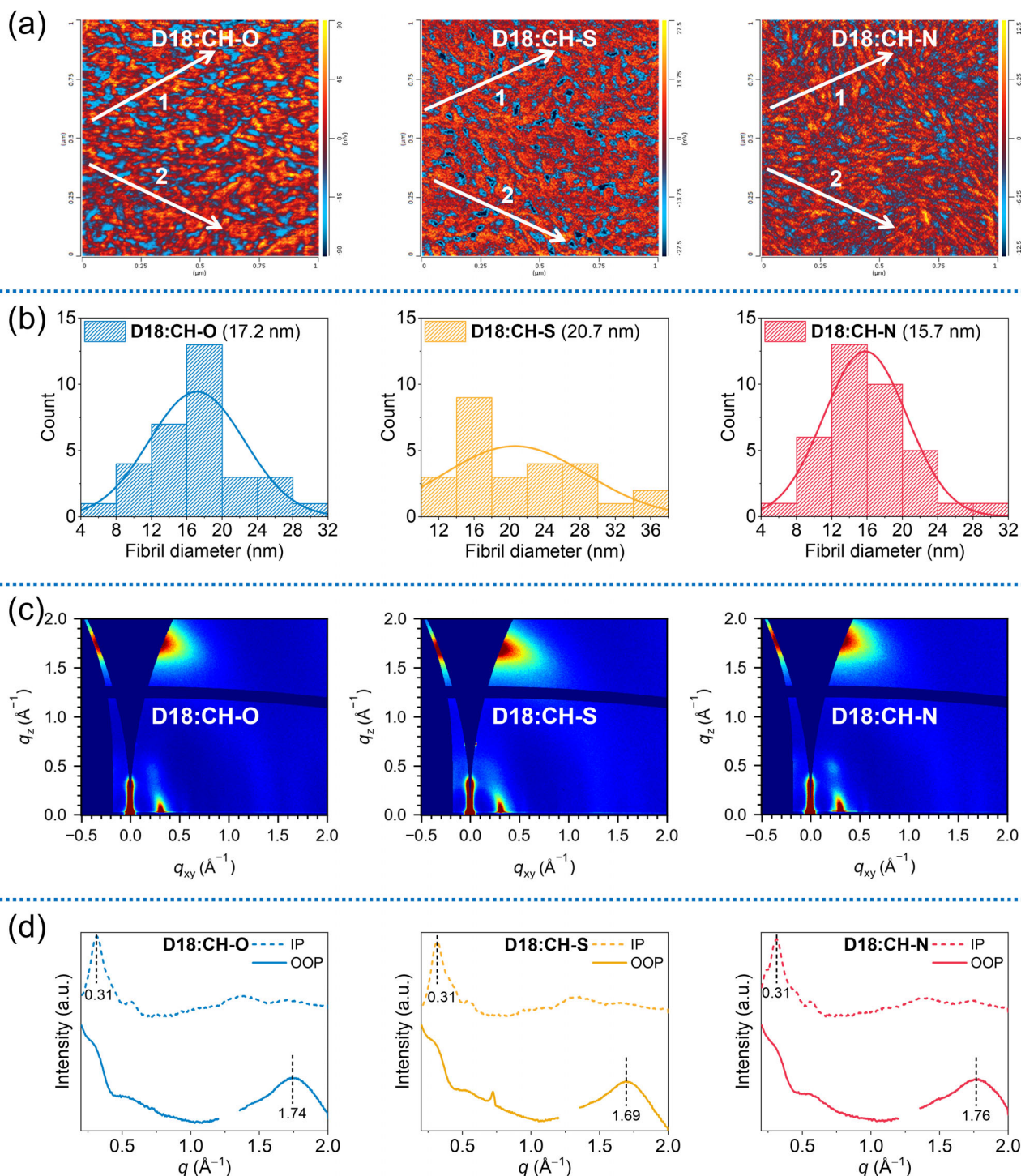


**Figure 6.** a) AFM-IR images of blended films. The donor and acceptor domains were marked with blue and red colors, respectively. b) Statistical fibril diameters in blended films. c) 2D GIWAXS patterns of blended films. d) Line-cut profiles of CH-O, CH-S, and CH-N blended films.

SLC method. As shown in Figure S23 (Supporting Information), the electron/hole mobility could be determined as 2.94/1.50, 3.09/2.01, and  $4.13/3.01 \times 10^{-4} \text{ cm}^2 \text{ V}^{-1} \text{ s}^{-1}$ , respectively, giving rise to the electron/hole mobility ratios of 1.96, 1.54 and 1.37. The larger and more balanced electron/hole mo-

bility of D18:CH-N blends should account for the better FF of D18:CH-N-based OSCs.<sup>[31]</sup> The largest  $\epsilon_r$  of D18:CH-N ( $\approx 6.0$ ) among three systems may be conducive to the more efficient charge transport in D18:CH-N blends (Figure S24, Supporting Information).

Note that the improvement of PCEs and FFs is closely related to the optimization of microstructure in D/A blended films.<sup>[32]</sup> Therefore, atomic force microscopy based infrared spectroscopy (AFM-IR) was further employed to study the morphology changes after switching O-, S-, and N-bridged on central cores. As displayed in **Figure 6a** and **Figure S25** (Supporting Information), all the three blends were characteristic of a relatively smooth film surface, indicated by a closing root-mean-square roughness ( $R_q$ ) of  $\approx 1.0$  nm. Then, we further recorded AFM-IR signals of blended films by detecting the stretching vibration of C $\equiv$ N bond in SMAs ( $2216\text{ cm}^{-1}$ ).<sup>[33]</sup> As shown in **Figure 6a**, it is obvious that D/A interpenetrating fibrillary networks can be observed, especially for D18:CH–N blend with a clearer D/A boundary. Additionally, transmission electron microscopy (TEM) images in **Figure S26** (Supporting Information) further verified this fibrillar micromorphology. The related literatures have revealed that the fibrillary morphology could accelerate charge migration effectively.<sup>[4c,34]</sup> By fine statistical analysis along the directions of the arrow, a reduced fiber size was observed in D18:CH–N (**Figure 6b**; **Figure S27**, Supporting Information), which is  $\approx 15.7$  nm comparing to  $\approx 17.2$  and  $\approx 20.7$  nm for D18:CH–O and D18:CH–S, respectively. The suitable phase separation for D18:CH–N should response for its superior charge transport (**Figure S23**, Supporting Information).

In light of the D/A phase separation size is greatly affected by the miscibility between donor and SMAs, the contact angles were tested and corresponding Flory-Huggins interaction parameters ( $\chi$ ) were calculated.<sup>[35]</sup> As shown in **Figure S28** and **Table S10** (Supporting Information), D18:CH–S possesses the largest  $\chi_{D:A}$  of 0.25, comparing to that of 0.09 for D18:CH–N and 0.16 for D18:CH–O. This suggests the better D/A miscibility for the relative planar SMAs containing dibenzodioxin and phenazine and agrees well with their relatively smaller phase separation. GIWAXS analysis of blended films has indicated the face-on molecular stacking orientation as same as the neat films (**Figure 6c**). Among them, CH–O and CH–N with the planar geometries have the smaller  $\pi$ – $\pi$  stacking distances but decreased CCL values comparing to D18:CH–S blends (**Figure 6d**; **Table S11**, Supporting Information). In short, although all of D18:CH–O, D18:CH–S, and D18:CH–N blends showed the fibrous morphology and achieved the excellent charge generation/transport,<sup>[36]</sup> the delicately tuning of crystallization properties of SMAs through bridged atom screening is still crucially important to determine the PCE difference of OSCs.

### 3. Conclusion

In order to expand the space for SMAs tailoring, O, S, and N atoms are adopted to bridge the 2D conjugated central cores on the same acceptor platform, yielding three SMAs of CH–O, CH–S, and CH–N. Due to the different  $p$ – $\pi$  orbital overlap between lone pair on O/S/N and the coterminous benzene planes, the central cores of SMAs have displayed quite different conformations and electronic properties, for example, planar and non-aromatic dibenzodioxin in CH–O, puckered and non-aromatic thianthrene in CH–S, planar and aromatic phenazine in CH–N. A systematic investigation disclosed the intrinsic photoelectronic properties of SMAs could be delicately tuned by the character of central units. For example, 1) the fully conjugation of central

unit in CH–O and CH–S was broken caused by the inefficient  $p$ – $\pi$  orbital overlap, which freezes the electron donating ability of aryl diol or dithiol moieties and results in the unexpectedly blue-shifted absorption of CH–O and CH–S comparing to CH–N, 2) the planar and aromatic phenazine in CH–N contributes to the larger dipole moment and polarizability, prolonged exciton lifetimes, more compact and ordered molecular packings, superior fibrillary D/A blending morphology and charge transport, etc., comparing to CH–O and CH–S. Benefitting from the advantages of phenazine, D18:CH–N-based binary OSCs achieved a first-class efficiency of 20.23% comparing to that of 18.48% for D18:CH–O and 18.93% for D18:CH–S. Note that CH–N has demonstrated a very few SMA skeleton besides the pathbreaking Y-series backbones (L8-BO and BTP-eC9, etc.), which could boost PCE of binary OSCs to surpass 20%. More excitingly, the highest FF of 83.13% in organic photovoltaics was also reached by D18:CH–N, manifesting the great potential for reducing FF gap between organic and inorganic photovoltaics through rational tailoring of central units in SMAs. By constructing these three SMAs, our work expands the structural scope of central units, moreover, provides valuable guidance to further central core construction.

### Supporting Information

Supporting Information is available from the Wiley Online Library or from the author.

### Acknowledgements

The authors gratefully acknowledge the financial support from the Ministry of Science and Technology of the People's Republic of China (National Key R&D Program of China, 2022YFB4200400), the National Natural Science Foundation of China (52025033, 51873089, 22204119, 22309090, 22474089), the Natural Science Foundation of Tianjin (23JCZDJC00140) and Haihe Laboratory of Sustainable Chemical Transformations.

### Conflict of Interest

The authors declare no conflict of interest.

### Author Contributions

X.C. and Z.X. contributed equally to this work. The synthetic works were carried out by Z.X. and J.G.; the device optimizations and measurements were carried out by X.C.; W.Z. and G.L. performed the DFT calculations. Y.C. and Z.Y. conceived and directed the study, and revised the manuscript. R.W., Y.Z., Y.G., and X.W. et al. helped to analyze the data and commented on the manuscript.

### Data Availability Statement

The data that support the findings of this study are available from the corresponding author upon reasonable request.

### Keywords

dibenzodioxin, organic photovoltaic, phenazine,  $p$ – $\pi$  conjugation, thianthrene

Received: February 15, 2025  
Revised: April 7, 2025  
Published online:

- [1] a) Y. Lin, J. Wang, Z.-G. Zhang, H. Bai, Y. Li, D. Zhu, X. Zhan, *Adv. Mater.* **2015**, *27*, 1170; b) W. Zhao, S. Li, H. Yao, S. Zhang, Y. Zhang, B. Yang, J. Hou, *J. Am. Chem. Soc.* **2017**, *139*, 7148; c) N. Qiu, H. Zhang, X. Wan, C. Li, X. Ke, H. Feng, B. Kan, H. Zhang, Q. Zhang, Y. Lu, Y. Chen, *Adv. Mater.* **2017**, *29*, 1604964; d) Y. Ma, M. Zhang, S. Wan, P. Yin, P. Wang, D. Cai, F. Liu, Q. Zheng, *Joule* **2021**, *5*, 197; e) Z. Wang, D. Zhang, L. Yang, O. Allam, Y. Gao, Y. Su, M. Xu, S. Mo, Q. Wu, Z. Wang, J. Liu, J. He, R. Li, X. Jia, Z. Li, L. Yang, M. D. Weber, Y. Yu, X. Zhang, T. J. Marks, N. Stingelin, J. Kacher, S. S. Jang, A. Facchetti, M. Shao, *Science* **2025**, *387*, 381; f) B. Jia, J. Wang, Y. Wu, M. Zhang, Y. Jiang, Z. Tang, T. P. Russell, X. Zhan, *J. Am. Chem. Soc.* **2019**, *141*, 19023.
- [2] a) J. Yuan, Y. Zhang, L. Zhou, G. Zhang, H.-L. Yip, T.-K. Lau, X. Lu, C. Zhu, H. Peng, P. A. Johnson, M. Leclerc, Y. Cao, J. Ulanski, Y. Li, Y. Zou, *Joule* **2019**, *3*, 1140; b) K. Jiang, Q. Wei, J. Y. L. Lai, Z. Peng, H. K. Kim, J. Yuan, L. Ye, H. Ade, Y. Zou, H. Yan, *Joule* **2019**, *3*, 3020; c) Y. Cui, H. Yao, J. Zhang, K. Xian, T. Zhang, L. Hong, Y. Wang, Y. Xu, K. Ma, C. An, C. He, Z. Wei, F. Gao, J. Hou, *Adv. Mater.* **2020**, *32*, 1908205; d) C. Li, J. Zhou, J. Song, J. Xu, H. Zhang, X. Zhang, J. Guo, L. Zhu, D. Wei, G. Han, J. Min, Y. Zhang, Z. Xie, Y. Yi, H. Yan, F. Gao, F. Liu, Y. Sun, *Nat. Energy* **2021**, *6*, 605; e) Y. Liang, D. Zhang, Z. Wu, T. Jia, L. Lüer, H. Tang, L. Hong, J. Zhang, K. Zhang, C. J. Brabec, N. Li, F. Huang, *Nat. Energy* **2022**, *7*, 1180; f) X. Jiang, S. Qin, L. Meng, G. He, J. Zhang, Y. Wang, Y. Zhu, T. Zou, Y. Gong, Z. Chen, G. Sun, M. Liu, X. Li, F. Lang, Y. Li, *Nature* **2024**, *635*, 860; g) Y. Zhang, W. Deng, C. E. Petoukhoff, X. Xia, Y. Lang, H. Xia, H. Tang, H. T. Chandran, S. Mahadevan, K. Liu, P. W. K. Fong, Y. Luo, J. Wu, S.-W. Tsang, F. Laquai, H. Wu, X. Lu, Y. Yang, G. Li, *Joule* **2024**, *8*, 509; h) C. Wang, X. Ma, Y.-f. Shen, D. Deng, H. Zhang, T. Wang, J. Zhang, J. Li, R. Wang, L. Zhang, Q. Cheng, Z. Zhang, H. Zhou, C. Tian, Z. Wei, *Joule* **2023**, *7*, 2386; i) C. Sun, J.-W. Lee, C. Lee, D. Lee, S. Cho, S.-K. Kwon, B. J. Kim, Y.-H. Kim, *Joule* **2023**, *7*, 416.
- [3] a) H. Chen, Y. Huang, R. Zhang, H. Mou, J. Ding, J. Zhou, Z. Wang, H. Li, W. Chen, J. Zhu, Q. Cheng, H. Gu, X. Wu, T. Zhang, Y. Wang, H. Zhu, Z. Xie, F. Gao, Y. Li, Y. Li, *Nat. Mater.* **2025**, *24*, 444; b) C. Li, J. Song, H. Lai, H. Zhang, R. Zhou, J. Xu, H. Huang, L. Liu, J. Gao, Y. Li, M. H. Jee, Z. Zheng, S. Liu, J. Yan, X.-K. Chen, Z. Tang, C. Zhang, H. Y. Woo, F. He, F. Gao, H. Yan, Y. Sun, *Nat. Mater.* **2025**, *24*, 433; c) Y. Sun, L. Wang, C. Guo, J. Xiao, C. Liu, C. Chen, W. Xia, Z. Gan, J. Cheng, J. Zhou, Z. Chen, J. Zhou, D. Liu, T. Wang, W. Li, *J. Am. Chem. Soc.* **2024**, *146*, 12011; d) L. Zhu, M. Zhang, G. Zhou, Z. Wang, W. Zhong, J. Zhuang, Z. Zhou, X. Gao, L. Kan, B. Hao, F. Han, R. Zeng, X. Xue, S. Xu, H. Jing, B. Xiao, H. Zhu, Y. Zhang, F. Liu, *Joule* **2024**, *8*, 3153; e) C. Chen, L. Wang, W. Xia, K. Qiu, C. Guo, Z. Gan, J. Zhou, Y. Sun, D. Liu, W. Li, T. Wang, *Nat. Commun.* **2024**, *15*, 6865.
- [4] a) Z. Yao, X. Cao, X. Bi, T. He, Y. Li, X. Jia, H. Liang, Y. Guo, G. Long, B. Kan, C. Li, X. Wan, Y. Chen, *Angew. Chem., Int. Ed.* **2023**, *62*, 202312630; b) Y.-J. Xue, Z.-Y. Lai, H.-C. Lu, J.-C. Hong, C.-L. Tsai, C.-L. Huang, K.-H. Huang, C.-F. Lu, Y.-Y. Lai, C.-S. Hsu, J.-M. Lin, J.-W. Chang, S.-Y. Chien, G.-H. Lee, U. S. Jeng, Y.-J. Cheng, *J. Am. Chem. Soc.* **2024**, *146*, 833; c) L. Zhu, M. Zhang, J. Xu, C. Li, J. Yan, G. Zhou, W. Zhong, T. Hao, J. Song, X. Xue, Z. Zhou, R. Zeng, H. Zhu, C. C. Chen, R. C. I. MacKenzie, Y. Zou, J. Nelson, Y. Zhang, Y. Sun, F. Liu, *Nat. Mater.* **2022**, *21*, 656.
- [5] a) Y. Shi, Y. Chang, K. Lu, Z. Chen, J. Zhang, Y. Yan, D. Qiu, Y. Liu, M. A. Adil, W. Ma, X. Hao, L. Zhu, Z. Wei, *Nat. Commun.* **2022**, *13*, 3256; b) Z. Luo, W. Wei, R. Ma, G. Ran, M. H. Jee, Z. Chen, Y. Li, W. Zhang, H. Y. Woo, C. Yang, *Adv. Mater.* **2024**, *36*, 2407517.
- [6] Z. Zhou, W. Liu, G. Zhou, M. Zhang, D. Qian, J. Zhang, S. Chen, S. Xu, C. Yang, F. Gao, H. Zhu, F. Liu, X. Zhu, *Adv. Mater.* **2019**, *32*, 1906324.
- [7] H. Liang, X. Bi, H. Chen, T. He, Y. Lin, Y. Zhang, K. Ma, W. Feng, Z. Ma, G. Long, C. Li, B. Kan, H. Zhang, O. A. Rakitin, X. Wan, Z. Yao, Y. Chen, *Nat. Commun.* **2023**, *14*, 4707.
- [8] a) K. Liu, Y. Jiang, F. Liu, G. Ran, F. Huang, W. Wang, W. Zhang, C. Zhang, J. Hou, X. Zhu, *Adv. Mater.* **2023**, *35*, 2300363; b) L. Yan, H. Zhang, Q. An, M. Jiang, A. Mahmood, M. H. Jee, H. R. Bai, H. F. Zhi, S. Zhang, H. Y. Woo, J. L. Wang, *Angew. Chem., Int. Ed.* **2022**, *61*, 202209454.
- [9] a) P. Li, X. Meng, K. Jin, Z. Xu, J. Zhang, L. Zhang, C. Niu, F. Tan, C. Yi, Z. Xiao, Y. Feng, G.-W. Wang, L. Ding, *Carbon Energy* **2023**, *5*, 250; b) H. Liu, Y. Geng, Z. Xiao, L. Ding, J. Du, A. Tang, E. Zhou, *Adv. Mater.* **2024**, *36*, 2404660.
- [10] a) H. Chen, Y. Zou, H. Liang, T. He, X. Xu, Y. Zhang, Z. Ma, J. Wang, M. Zhang, Q. Li, C. Li, G. Long, X. Wan, Z. Yao, Y. Chen, *Sci. China Chem.* **2022**, *65*, 1362; b) W. Wei, C. e. Zhang, Z. Chen, W. Chen, G. Ran, G. Pan, W. Zhang, P. Müller-Buschbaum, Z. Bo, C. Yang, Z. Luo, *Angew. Chem., Int. Ed.* **2024**, *63*, 202315625; c) Z. Wang, M. Ji, A. Tang, M. Du, C. Mu, Y. Liu, E. Wang, E. Zhou, *Energy Environ. Sci.* **2024**, *17*, 3868; d) H. Fang, Q. Chen, Y. Lin, X. Xu, J. Wang, M. Li, C. Xiao, C. R. McNeill, Z. Tang, Z. Lu, W. Li, *Angew. Chem., Int. Ed.* **2025**, *64*, 202417951.
- [11] a) H. Chen, H. Liang, Z. Guo, Y. Zhu, Z. Zhang, Z. Li, X. Cao, H. Wang, W. Feng, Y. Zou, L. Meng, X. Xu, B. Kan, C. Li, Z. Yao, X. Wan, Z. Ma, Y. Chen, *Angew. Chem., Int. Ed.* **2022**, *61*, 202209580; b) T. Xu, Z. Luo, R. Ma, Z. Chen, T. A. Dela Peña, H. Liu, Q. Wei, M. Li, C. e. Zhang, J. Wu, X. Lu, G. Li, C. Yang, *Angew. Chem., Int. Ed.* **2023**, *62*, 202304127.
- [12] a) N. Wei, J. Chen, Y. Cheng, Z. Bian, W. Liu, H. Song, Y. Guo, W. Zhang, Y. Liu, H. Lu, J. Zhou, Z. Bo, *Adv. Mater.* **2024**, *36*, 2408934; b) B. Fan, H. Gao, L. Yu, R. Li, L. Wang, W. Zhong, Y. Wang, W. Jiang, H. Fu, T. Chen, B. Kan, S.-W. Tsang, A. K.-Y. Jen, *Angew. Chem., Int. Ed.* **2025**, *64*, 202418439; c) S. Guan, Y. Li, C. Xu, N. Yin, C. Xu, C. Wang, M. Wang, Y. Xu, Q. Chen, D. Wang, L. Zuo, H. Chen, *Adv. Mater.* **2024**, *36*, 2400342; d) Z. Chen, J. Ge, W. Song, X. Tong, H. Liu, X. Yu, J. Li, J. Shi, L. Xie, C. Han, Q. Liu, Z. Ge, *Adv. Mater.* **2024**, *36*, 2406690.
- [13] a) Z. Zhang, Y. Li, G. Cai, Y. Zhang, X. Lu, Y. Lin, *J. Am. Chem. Soc.* **2020**, *142*, 18741; b) F. Lin, K. Jiang, W. Kaminsky, Z. Zhu, A. K. Y. Jen, *J. Am. Chem. Soc.* **2020**, *142*, 15246; c) F. Huang, Z. Li, G. Song, C. Jiang, Y. Yang, J. Wang, X. Wan, C. Li, Z. Yao, Y. Chen, *Adv. Funct. Mater.* **2023**, *33*, 2211140.
- [14] a) H. Huang, L. Yang, A. Facchetti, T. J. Marks, *Chem. Rev.* **2017**, *117*, 10291; b) J. Hai, Y. Song, L. Li, X. Liu, X. Shi, Z. Huang, G. Qian, Z. Lu, J. Yu, H. Hu, S. Chen, *Adv. Funct. Mater.* **2023**, *33*, 2213429.
- [15] S. I. Etkind, T. M. Swager, *Synthesis* **2022**, *54*, 4843.
- [16] S. Kim, Y. Kwon, J.-P. Lee, S.-Y. Choi, J. Choo, *J. Mol. Struct.* **2003**, *655*, 451.
- [17] a) X. Wan, C. Li, M. Zhang, Y. Chen, *Chem. Soc. Rev.* **2020**, *49*, 2828; b) G. Li, F. Qin, R. M. Jacobberger, S. Mukherjee, L. O. Jones, R. M. Young, R. M. Pankow, B. P. Kerwin, L. Q. Flagg, D. Zheng, L.-W. Feng, K. L. Kohlstedt, V. K. Sangwan, M. C. Hersam, G. C. Schatz, D. M. DeLongchamp, M. R. Wasielewski, Y. Zhou, A. Facchetti, T. J. Marks, *Joule* **2023**, *7*, 2152.
- [18] a) Z. Chen, Y. Xiao, H. Yao, J. Ren, T. Zhang, J. Qiao, S. Zhu, R. Lin, X. Hao, J. Hou, *Adv. Mater.* **2024**, *36*, 2408858; b) X. Cao, P. Wang, X. Jia, W. Zhao, H. Chen, Z. Xiao, J. Li, X. Bi, Z. Yao, Y. Guo, G. Long, C. Li, X. Wan, Y. Chen, *Angew. Chem., Int. Ed.* **2025**, *137*, 202417244.
- [19] Z. Xu, X. Cao, Z. Yao, W. Zhao, W. Shi, X. Bi, Y. Li, Y. Guo, G. Li, G. Long, X. Wan, C. Li, Y. Chen, *Angew. Chem., Int. Ed.* **2025**, <https://doi.org/10.1002/anie.202421289>.
- [20] W. Zhu, A. P. Spencer, S. Mukherjee, J. M. Alzola, V. K. Sangwan, S. H. Amsterdam, S. M. Swick, L. O. Jones, M. C. Heiber, A. A. Herzing, G. Li, C. L. Stern, D. M. DeLongchamp, K. L. Kohlstedt, M. C. Hersam,

- G. C. Schatz, M. R. Wasielewski, L. X. Chen, A. Facchetti, T. J. Marks, *J. Am. Chem. Soc.* **2020**, *142*, 14532.
- [21] J. Bertrandie, J. Han, C. S. P. De Castro, E. Yengel, J. Gorenflot, T. Anthopoulos, F. Laquai, A. Sharma, D. Baran, *Adv. Mater.* **2022**, *34*, 2202575.
- [22] Z. Xu, S. Li, F. Huang, T. He, X. Jia, H. Liang, Y. Guo, G. Long, B. Kan, Z. Yao, C. Li, X. Wan, Y. Chen, *Angew. Chem., Int. Ed.* **2023**, *62*, 202311686.
- [23] a) M. Más-Montoya, R. A. J. Janssen, *Adv. Funct. Mater.* **2017**, *27*, 1605779; b) H. Lu, D. Li, W. Liu, G. Ran, H. Wu, N. Wei, Z. Tang, Y. Liu, W. Zhang, Z. Bo, *Angew. Chem., Int. Ed.* **2024**, *63*, 202407007.
- [24] S. Kumar, I. S. Dunn, S. Deng, T. Zhu, Q. Zhao, O. F. Williams, R. Tempelaar, L. Huang, *Nat. Chem.* **2023**, *15*, 1118.
- [25] A. J. Gillett, A. Privitera, R. Dilmurat, A. Karki, D. Qian, A. Pershin, G. Londi, W. K. Myers, J. Lee, J. Yuan, S.-J. Ko, M. K. Riede, F. Gao, G. C. Bazan, A. Rao, T.-Q. Nguyen, D. Beljonne, R. H. Friend, *Nature* **2021**, *597*, 666.
- [26] P. K. Nayak, *Synth. Met.* **2013**, *174*, 42.
- [27] Q. Liu, Y. Jiang, K. Jin, J. Qin, J. Xu, W. Li, J. Xiong, J. Liu, Z. Xiao, K. Sun, S. Yang, X. Zhang, L. Ding, *Sci. Bull.* **2020**, *65*, 272.
- [28] K. Jiang, J. Zhang, C. Zhong, F. R. Lin, F. Qi, Q. Li, Z. Peng, W. Kaminsky, S.-H. Jang, J. Yu, X. Deng, H. Hu, D. Shen, F. Gao, H. Ade, M. Xiao, C. Zhang, A. K. Y. Jen, *Nat. Energy* **2022**, *7*, 1076.
- [29] a) Y. Jiang, K. Liu, F. Liu, G. Ran, M. Wang, T. Zhang, R. Xu, H. Liu, W. Zhang, Z. Wei, Y. Cui, X. Lu, J. Hou, X. Zhu, *Adv. Mater.* **2025**, *37*, 2500282; b) Y. Jiang, S. Sun, R. Xu, F. Liu, X. Miao, G. Ran, K. Liu, Y. Yi, W. Zhang, X. Zhu, *Nat. Energy* **2024**, *9*, 975.
- [30] a) L. J. A. Koster, V. D. Mihailetschi, R. Ramaker, P. W. M. Blom, *Appl. Phys. Lett.* **2005**, *86*, 123509; b) M. Lenes, M. Morana, C. J. Brabec, P. W. M. Blom, *Adv. Funct. Mater.* **2009**, *19*, 1106.
- [31] Y. Liu, T. P. Russell, *Acc. Chem. Res.* **2022**, *55*, 1097.
- [32] a) X. Zhang, C. Li, J. Xu, R. Wang, J. Song, H. Zhang, Y. Li, Y.-N. Jing, S. Li, G. Wu, J. Zhou, X. Li, Y. Zhang, X. Li, J. Zhang, C. Zhang, H. Zhou, Y. Sun, Y. Zhang, *Joule* **2022**, *6*, 444; b) C. Chen, L. Wang, Y. Sun, Y. Fu, C. Guo, B. Zhou, Z. Gan, D. Liu, W. Li, T. Wang, *Adv. Funct. Mater.* **2023**, *33*, 2305765; c) L. Kong, Z. Zhang, N. Zhao, Z. Cai, J. Zhang, M. Luo, X. Wang, M. Chen, W. Zhang, L. Zhang, Z. Wei, J. Chen, *Adv. Energy Mater.* **2023**, *13*, 2300763.
- [33] J. Song, C. Li, H. Ma, B. Han, Q. Wang, X. Wang, D. Wei, L. Bu, R. Yang, H. Yan, Y. Sun, *Adv. Mater.* **2024**, *36*, 2406922.
- [34] a) F. Zhao, C. Wang, X. Zhan, *Adv. Energy Mater.* **2018**, *8*, 1703147; b) P. Bi, S. Zhang, Z. Chen, Y. Xu, Y. Cui, T. Zhang, J. Ren, J. Qin, L. Hong, X. Hao, J. Hou, *Joule* **2021**, *5*, 2408.
- [35] S. Nilsson, A. Bernasik, A. Budkowski, E. Moons, *Macromolecules* **2007**, *40*, 8291.
- [36] D. Hu, H. Tang, C. Chen, D.-J. Lee, S. Lu, G. Li, H.-Y. Hsu, F. Laquai, *Adv. Mater.* **2024**, *36*, 2406949.